Highly Efficient Unitized Regenerative Hydrogen Peroxide Cycle Cell with Ultra-Low Overpotential for Renewable Energy Storage

Jie Yang[1,2], Ruimin Ding[1], Chang Liu[1,2], Shanshan Liu[1], Qinchao Xu[1], Lifang Chen[1], Jingchao Chen[1], Junfen Li[1], Xi Yin[1]*

Affiliations:

[1]State Key Laboratory of Coal Conversion, Institute of Coal Chemistry, Chinese Academy of Sciences; Taiyuan, Shanxi 030001, China.

[2]School of Chemical Engineering, University of Chinese Academy of Sciences; Beijing 100049, China.

*Corresponding author. Email: xiyin@sxicc.ac.cn

Abstract

Future large-scale application of intermittent renewable sourced energy requires low cost, efficient, and less resource-demanding energy storage systems for grid balancing. Conventional unitized regenerative fuel cells (URFCs) based on the water-H_2 cycle are promising but suffer from high overpotential and low energy efficiency. Herein, we demonstrate a highly efficient unitized regenerative hydrogen peroxide (H_2O_2) cycle cell (UR-HPCC) for renewable energy storage. The prototype utilized a carbon-based platinum group metal-free (PGM-free) catalyst with atomically dispersed Co and N dopants (Co-N-C) as the bifunctional oxygen electrode catalyst for the hydrogen peroxide oxidation reaction (HPOR) and two-electron oxygen reduction reaction (2e-ORR) in H_2O_2 electrolyzer and fuel cell modes, respectively. This prototype showed a close-to-zero overpotential with a remarkably high round-trip efficiency of over 90%, which was attributed to the ideal catalytic properties of Co-N-C toward HPOR and 2e-ORR. Thermodynamic analysis of the above single-intermediate reactions suggests the intrinsic supremacy of UR-HPCC in energy

efficiency and reversibility over conventional URFCs, paving the road to future sustainable distributed generation and energy storage systems.

Keywords Unitized regenerative fuel cell, hydrogen peroxide cycle cell, PGM-free catalyst, energy storage

Future wide-scale installation of renewable electricity, such as wind and solar power, demands flexible distributed energy storage systems to balance the grid power fluctuation between peak and off-peak hours.[1,2] Unitized regenerative fuel cells (URFCs), as one promising energy storage technology, integrate the functions of water electrolyzer (WE) and hydrogen fuel cell (FC).[1-4] When excess electricity is available, the URFCs operate in WE mode and electrolyze water into hydrogen and oxygen to store electrical energy. At night, or when additional baseload power is required to supplement solar and wind, the URFCs operate in FC mode and generate electric power while converting hydrogen back to the water. The numerous advantages of URFCs, including reduced hardware cost, flexibility and fast response for grid balancing, and clean H_2-water cycle operation, render it highly attractive.[1-4] However, to be considered for the renewable energy storage system, current URFCs must reduce the overpotential originating from the sluggish oxygen reduction reaction (ORR) and oxygen evolution reactions (OER) at the same time to achieve a high round-trip efficiency (RTE).[4-6] While drastic progress has been made in this field, the state-of-the-art proton exchange membrane (PEM) URFCs are still far from reaching zero overpotential and 100% energy efficiency.[4,7-9]

To date, the onset overpotential for ORR in FC mode (η_{FC}) and for OER in WE mode (η_{WE}) are typically *ca*. 0.2 V, which adds up to a total onset overpotential (η_{total}) of *ca*. 0.4 V in PEM URFC.[4,10] The high overpotential in PEM URFC yields a low RTE of 40-60%.[7-9] In addition, the use of precious metal-based catalysts for OER and ORR, such as iridium and platinum, also increases the cost of PEM URFCs systems.[5,11-13] The complicated multistep ORR/OER mechanisms, the scaling relationship of the

thermodynamic barriers along the reaction pathways, and the lack of ideal catalytic materials make it extremely challenging, if all possible, to further reduce the overpotential in the current water-H_2 cycle PEM URFC systems. [14-17]

Recently, we proposed to empower the electrochemical synthesis and electrolysis of H_2O_2 for distributed energy storage and demonstrated a highly efficient PEM hydrogen peroxide electrolyzer (HPEL) for power-to-hydrogen conversion.[18] However, to the best of our knowledge, the concept of energy storage based on the electrochemical cycle of H_2O_2 has not been demonstrated in the URFC-type devices.

Herein we propose a revolutionary design of PEM URFC based on the electrochemical cycle of hydrogen peroxide, namely unitized regenerative hydrogen peroxide cycle cell (UR-HPCC) (**Figure 1**). The proposed UR-HPCC can operate in either hydrogen peroxide electrolyzer (HPEL) mode to store the "off-peak" electricity from solar or wind farms, or in fuel cell (FC) mode to generate electricity at the peak hour. In HPEL mode, the device splits H_2O_2 and produces H_2/O_2 through hydrogen peroxide oxidation reaction (HPOR: $H_2O_2 \rightarrow O_2 + 2e^- + 2H^+$, $E^0 = 0.695$ V *vs*. SHE) and hydrogen evolution reaction (HER: $2H^+ + 2e^- \rightarrow H_2$, $E^0 = 0$ V *vs*. SHE), storing electric energy in the form of hydrogen fuel. In FC mode, the UR-HPCC utilizes the H_2 and O_2 to generate electricity while producing H_2O_2 via hydrogen oxidation reaction (HOR: $H_2 \rightarrow 2e^- + 2H^+$, $E^0 = 0$ V *vs*. SHE) and two-electron oxygen reduction reaction (2e-ORR: $O_2 + 2e^- + 2H^+ \rightarrow H_2O_2$, $E^0 = 0.695$ V *vs*. SHE). This UR-HPCC utilized a constant gas electrode design, where HPOR and 2e-ORR occur in the oxygen electrode while HER and HOR occur in the hydrogen electrode, allowing fast switching between HPEL and FC modes without the risk of mixing H_2 and O_2. The thermodynamic equilibrium potential for HPOR/2e-ORR (0.695 V *vs* SHE) is much lower than that for OER/ORR and makes quite a large selection of low-cost materials available to be used as the oxygen electrode catalyst and bipolar plates in UR-HPCC. Most importantly, unlike the limiting potentials of OER and ORR which are restricted by the scaling relationships of the intermediates' binding energy on catalyst surface, the limiting

potential for HPOR and 2e-ORR can reach the thermodynamic equilibrium potential of 0.695 V, making it possible to reach the ultimate zero-overpotential operation for UR-HPCC.[14-17]

As a proof-of-concept, we demonstrate a highly efficient PEM UR-HPCC by employing a bifunctional PGM-free Co-N-C catalysts for HPOR and 2e-ORR in the oxygen electrode. Without the restrictions of scaling relationships of reaction intermediates, this UR-HPCC achieved a maximum voltage efficiency of over 98% when operating in HPEL and FC modes and a maximum RTE of *ca*. 95.8% at low current density in UR-HPCC mode. This prototype also demonstrated decent stability with RTE maintained above *ca*. 79.7% after 15 charge-discharge cycles in 30 h. The ultra-low overpotential, remarkably high energy efficiency, and decent cyclability of UR-HPCC rooted in its supreme thermodynamics pave the road to the future large-scale distributed generation and energy storage systems based on the electrochemical cycle of H_2O_2.

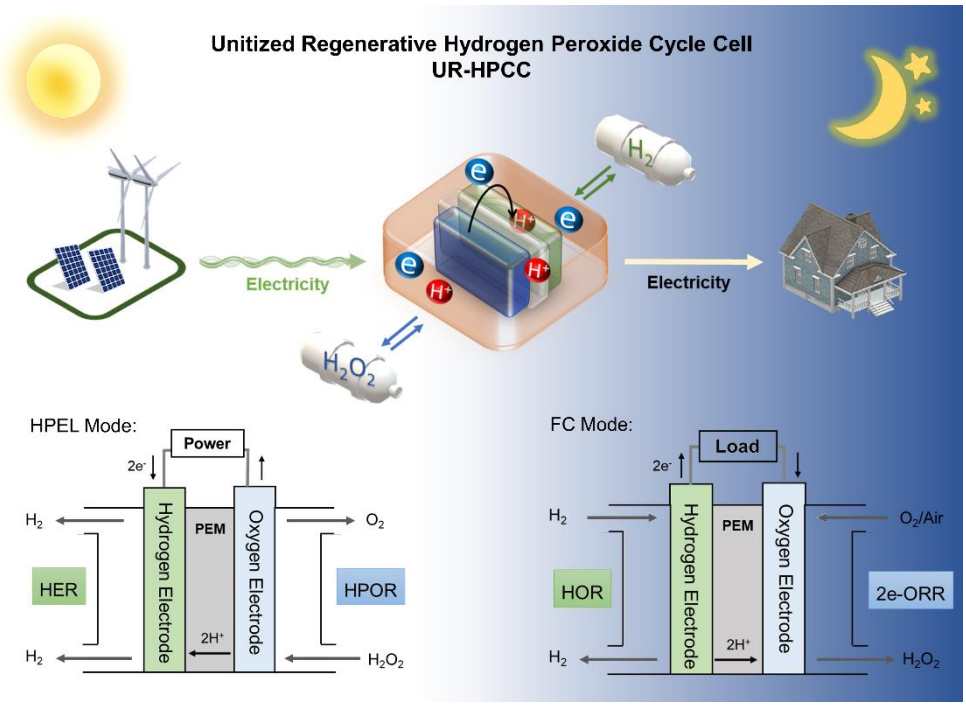

Figure 1. Schematic diagram of UR-HPCC system for renewable energy storage and grid balancing. The system converts and stores electricity from wind and solar power in the form of hydrogen by splitting H_2O_2 in HPEL mode at "off-peak" hour and generate electric power in FC mode by converting H_2 to H_2O_2 at peak hour.

Synthesis and characterization of bifunctional atomically dispersed Co-N-C electrocatalyst

We synthesized a bifunctional Co-N-C catalyst by pyrolysis of a precursor mixture containing cobalt chloride ($CoCl_2$), polyaniline (PANI), and oxidized carbon black (OCB), followed by acid-leaching and a second heat-treatment (See detailed synthesis procedures in the Method section). This synthesis method differs from previous PANI-based synthesis approaches by introducing H_2O_2 as a clean oxidizer instead of ammonia persulfate, effectively avoiding metal sulfide formation. The X-ray diffraction pattern (XRD) pattern of the obtained Co-N-C catalyst shows only two distinct characteristic peaks at approximately 26.54° and 43.28°, which are ascribed to the (002) and (101) planes of graphite phase (PDF #57-1621) (**Figure 2a**). No diffraction peaks from metal-rich phases were observed. The Co-N-C catalyst's surface compositions and electronic states were analyzed by X-ray photoelectron spectroscopy (XPS). The estimated atomic percentage contents of N, O, and Co in the catalysts are 3.73 at.%, 4.76 at.%, and 0.27 at.%, respectively. The high-resolution N 1s XPS spectrum (Figure 2b) can be deconvoluted into five contributions, including pyridinic-N (398.3 eV), Co-N_x (399.5 eV), pyrrolic-N (400.9 eV), graphitic-N (401.9 eV), and oxide-N (403.2 eV).[19] In addition, the high-resolution Co 2p spectrum can be divided into the $2p_{1/2}$ and $2p_{3/2}$ regions. The main peaks in the Co $2p_{3/2}$ region are 780.9 eV and 782.9 eV and can be ambiguously assigned to either the Co^{2+} or the Co^{3+} oxidation states (Figure 2c).[20] The transmission electron microscopy (TEM) image shows the uniform carbon nanostructures without any Co-rich particles (Figure 2d). And the associated energy dispersive spectroscopy (EDS) elemental mapping (Figure 2e) showed the distinguishable signals of C, N, and Co, revealing the densely and uniformly dispersed Co atoms on the carbon matrix. The obtained Co-N-C catalyst was further characterized using aberration-corrected high-angle annular dark-field scanning TEM (HAADF-STEM). The STEM micrograph confirms isolated Co atoms distributed in the nitrogen-doped carbon matrix shown as the bright spots (Figure 2f). The above results indicate

that the catalyst structure is a Co-N_x molecule with Co atoms atomically dispersed in a nitrogen-doped carbon matrix.

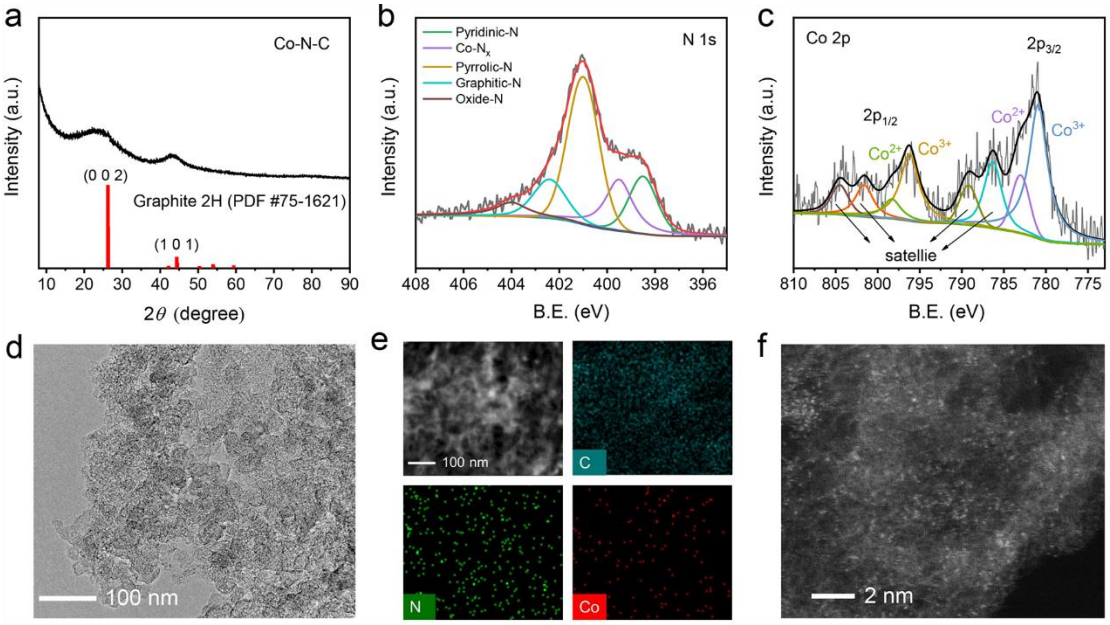

Figure 2. Characterization of Co-N-C catalyst. (a) XRD pattern, (b) N1s XPS spectrum, (c) Co 2p XPS spectrum, (d) TEM micrograph, (e) EDS elemental mapping, and (f) HAADF-STEM micrograph of atomically dispersed Co-N-C catalyst.

Electrocatalytic activity of the bifunctional Co-N-C catalyst for HPOR and 2e-ORR

The synthesized Co-N-C catalyst showed high catalytic activity for both HPOR and 2e-ORR during the electrochemical test (**Figure 3**). When being polarized in a mixed electrolyte of 0.5 M H_2SO_4 and 0.5 M H_2O_2, the Co-N-C showed an onset potential of *ca*. 0.71 V *vs*. RHE for the HPOR, and the HPOR current further increased with the potential and achieved a current density of 300 mA cm^{-2} at 1.0 V *vs*. RHE (Figure 3a). When polarized from 1 V to 0 V in O_2-saturated 0.5 M H_2SO_4 solution, Co-N-C catalyst showed a high onset potential of *ca*. 0.75 V *vs*. RHE for 2e-ORR judged by the onset potential of ring-current. It also demonstrated a high selectivity for 2e-ORR between 0.6 V and 0.3 V *vs*. RHE with a hydrogen peroxide yield (Y_{H2O2}) of 65% to 60%, which decreased to *ca*. 35% when the potential decreased to 0 V (Figure 3a and **Figure S1**). In comparison, oxidized carbon black (OCB) and nitrogen-doped carbon

(N-C) showed low activity for both HPOR and 2e-ORR (**Figure S1**), suggesting that Co-N_x moieties are the active sites for HPOR and 2e-ORR.

We attributed the excellent HPOR and 2e-ORR activity of Co-N-C catalyst to the ideal binding energy of HOO* intermediate at Co-N_4 sites. Previous computational works suggested that Co-N_4 sites are active for 2e-ORR in acid.[21-24] The predictated binding energy of hydroperoxyl intermediate (ΔG_{HOO*}) at pyrolic-N coordinated Co-N_4 site is 4.24 eV, and the corresponding free energy is 3.54 eV at 0.7 V, 0.02 eV away from the ideal value of 3.52 eV (Figure 3c).[22] Since HPOR is the reverse reaction of 2e-ORR and shares the same single intermetiate of HOO*, the thermodynamic energy barrier for both HPOR and 2e-ORR are the same 0.02 eV, and these Co-N_x sites should be very active for both reactions as shown above in our work. Correspondingly, the predicted limiting potential for HPOR should be 0.715 V *vs*. RHE at standard conditions (pH = 1, 1 M H_2O_2 solution), which is in good agreement with our experimental data.

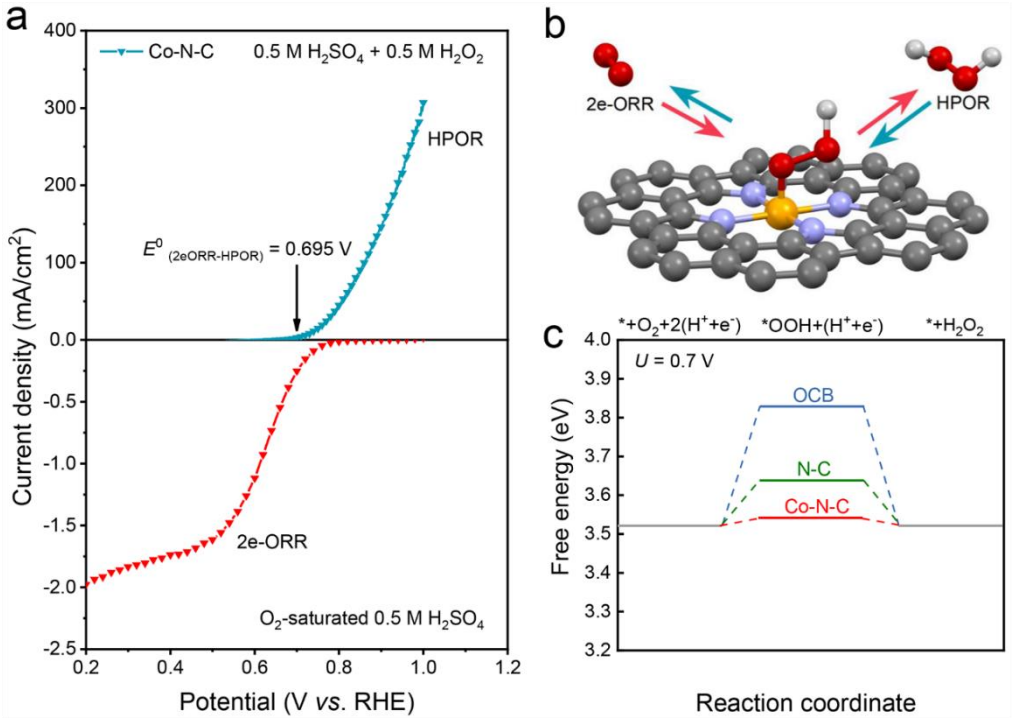

Figure 3. Bifunctionality of Co-N-C catalyst for HPOR and 2e-ORR. (a) HPOR polarization curve in 0.5 M H_2SO_4 and 0.5 M H_2O_2, and 2e-ORR polarization curve in O_2-saturated 0.5 M H_2SO_4 at 900 rpm, 25 °C. Catalyst loading was 0.1 mg/cm^2. (b)

Schematic of HPOR and 2e-ORR pathways catalyzed by Co-N_4 site. (c) Free energy diagram of HPOR/2e-ORR with HOO* intermediate at Co-N-C, N-C, and OCB.[22,25,26]

Performance of UR-HPCC

The membrane electrode assembly (MEA) of the UR-HPCC was fabricated using Co-N-C catalyst on carbon cloth as the oxygen electrode, a commercial Pt/C catalyst on carbon paper as the hydrogen electrode, and Nafion NR211 membrane. A hydrophilic carbon cloth substrate was used as the porous transport layer of the oxygen electrode to balance performance between FC and HPEL mode. The detailed membrane electrode assembly (MEA) fabrication method and cell hardware are described in the Method section and shown in the Supplementary materials (**Figure S2 and S3**).

The performance of the UR-HPCC was first evaluated in discrete HPEL mode and FC mode. **Figure 4a** shows the polarization curve of the cell in discrete HPEL mode. Due to the high HPOR activity of Co-N-C catalyst, the cell's open-circuit voltage (OCV) in HPEL mode was *ca*. 0.712 V, with an overpotential (η_{HPEL}) of only 8 mV relative to the theoretical voltage of 0.704 V in 0.5 M H_2O_2 and 0.5 M H_2SO_4 solution. The voltage efficiency (VE_{HPEL}) remained above 70% at voltage below 1.0 V. The maximum VE_{HPEL} of 98% can be achieved at OCV thanks to the low overpotential. When the internal resistance-corrected cell voltage ($E_{iR\text{-free}}$) increased from 0.7 to 1.0 V, the charging current density (j) increased monotonically to *ca*. 276 mA cm^{-2}. Correspondingly, the hydrogen generation rate (r_{H2}) increased from 1.34 mmol cm^{-2} h^{-1} to 4.74 mmol cm^{-2} h^{-1}, and the Faraday efficiency for HER (FE_{H2}) increases from *ca*. 83.41% to 96.16% (**Figure 4b**). The FE_{H2} is less than 100% due to the reduction of crossover H_2O_2 ($HPRR_{crossover}$, $H_2O_2 + 2H^+ + 2e^- \rightarrow 2H_2O$, E_0 = 1.78 V *vs*. RHE) at the hydrogen electrode. The increase of FE_{H2} with cell voltage is attributed to the acceleration of HPOR and inhibition of the H_2O_2 crossover to the hydrogen electrode (**Figure S4**, see Supplementary Information for details).[18] During the stability test at a constant current of 50 mA/cm^2, the E_{cell} increased from *ca*. 0.876 to 1.0 V in 52 h at an average rate of

2.38 mV/h, showing the excellent stability of the cell in discrete HPEL mode (**Figure 4c**).

Figure 4a also shows the polarization curve of UR-HPCC in discrete H_2-O_2 FC mode at room temperature. The cell showed an OCV of *ca*. 0.693 V, corresponding to η_{FC} of 2 mV. The current density increased as the discharge voltage decreased and reached *ca*. 278 mA/cm^2 at 0.25 V. The H_2O_2-generation rate (r_{H2O2}) is 0.09 mmol/(cm^2 h) at 0.6 $V_{iR\text{-free}}$, and the corresponding Faradaic efficiency for H_2O_2 synthesis (FE_{H2O2}) is 62.8% (**Figure 4b**, and see Supplementary Information for additional discussion). The r_{H2O2} in FC mode increased with discharge current and reached 0.45 mmol/ (cm^2 h) at 0.3 V, but the corresponding FE_{H2O2} decreased to *ca*. 13.4%. We attributed the decrease of FE_{H2O2} with cell voltage to the reduction of produced H_2O_2, like the potential dependency of Y_{H2O2} observed on RRDE (**Figure S1d**). In a 52-hour test at 50 mA/cm^2, the E_{cell} decreased from 0.46 to 0.3 V with a rate of 3.0 mV/h, showing an excellent stability during the continuous operation in FC mode (**Figure 4c**).

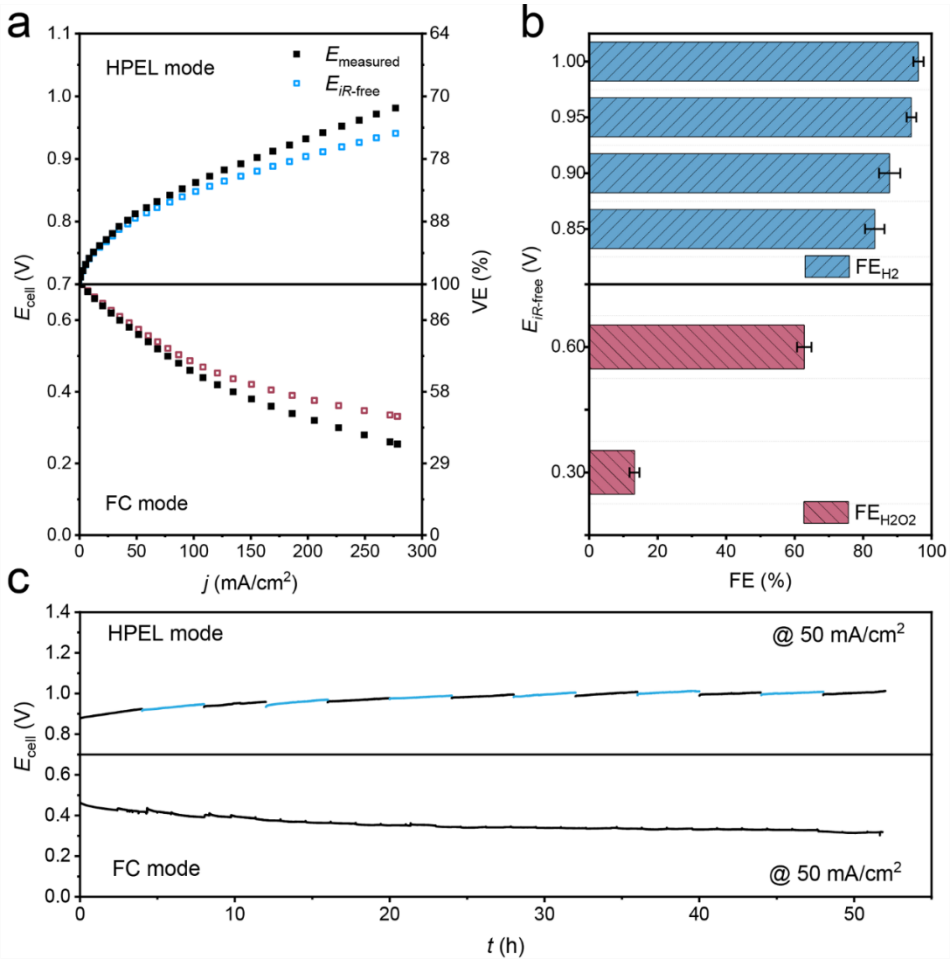

Figure 4. Performance of the UR-HPCC with PGM-free bifunctional Co-N-C catalyst on the oxygen electrode in discrete HPEL and FC modes. (a) Polarization and voltage efficiency curves. (b) Faradaic efficiency for hydrogen generation (FE_{H2}) and for H_2O_2 synthesis (FE_{H2O2}) in HPEL and FC modes, respectively. (c) Stability of UR-HPCC in discrete HPEL and FC modes at a constant current density of 50 mA/cm^2. See Method Section for experimental details.

The UR-HPCC showed a remarkable low overpotential, decent cyclability, and good stability during a 30-h test (**Figure 5**). The initial OCV was *ca*. 0.71 V and 0.69 V for HPEL mode and FC mode, and the total overpotential ($\eta_{total} = \eta_{FC} + \eta_{HPEL}$) was only 0.02 V, which is consistent with that in discrete modes. Starting from HPEL mode, the first pol-curves in HPEL and FC modes are close to those measured in discrete mode, indicating the high cyclability of the UR-HPCC in the first cycle. In 15 cycles, the polarization curves shifted gradually with a decrease in current density and then

stabilized after 10 cycles. After 15 cycles, the η_{total} increased to *ca*. 0.11 V, which is still low enough to provide a high votage efficiency. Figure 5b presents the change of cell voltage at 50 mA/cm^2 during the 30-hour cyclability test. In the HPEL mode, the charge voltage at 50 mA/cm^2 increased from *ca*. 0.81 to 0.89 V after 15 cycles. And the discharge voltage at 50 mA/cm^2 in FC mode decreased from *ca*. 0.53 to 0.36 V. The stability of UR-HPCC is similar to that in discret HPEL and FC mode, suggesting that the duty cycle did not accelerate the performance degradation. Eventually, the charge-discharge voltage stablized after 10 cycels, showing good stability of the cell in UR-HPCC mode (**Figure 5b**).

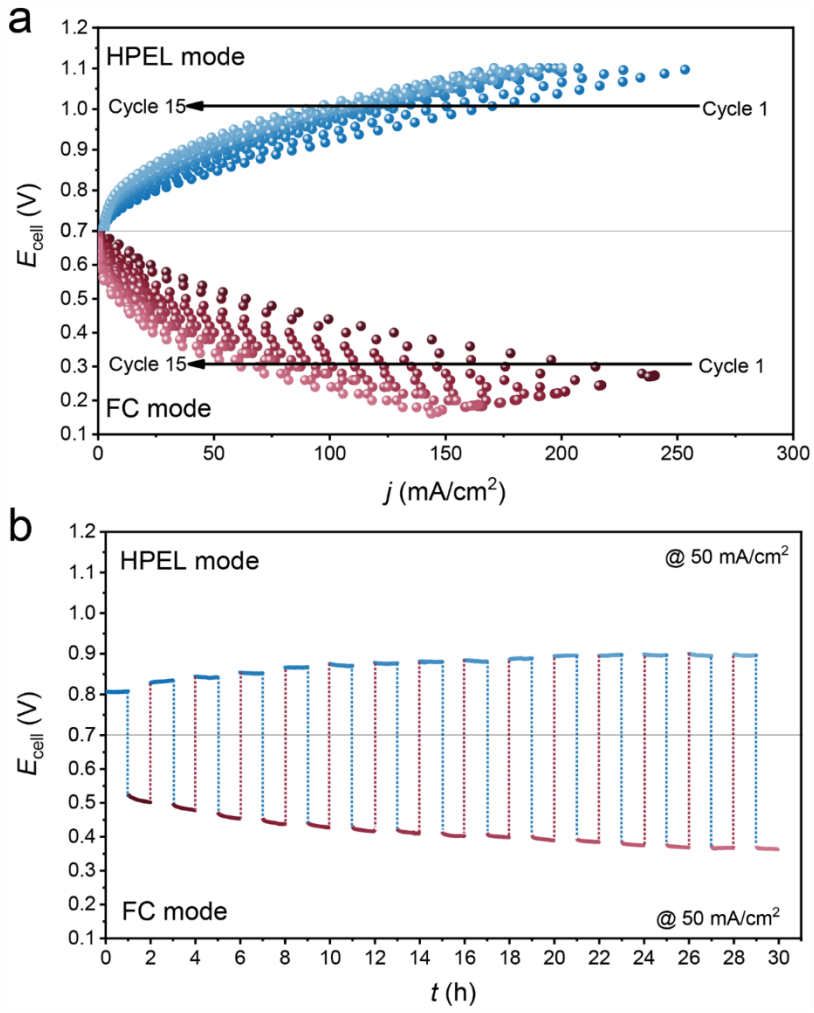

Figure 5. The performance of UR-HPCC during the cyclability test. (a) Polarization curves in 15 cycles. (b) Change of cell voltage in 30 h stability measurement using galvanostatic method at 50 mA/cm^2. See Method Section for experimental details.

Figure 6a shows the 2D contour plot of RTE as a function of cell voltages in HPEL and FC mode (E_{HPEL} and E_{FC}) in the first cycle, where RTE = E_{FC}/E_{HPEL}. With the extremely low η_{total}, this UR-HPCC showed a facinatingly high RTE of up to 99.6%, much higher than that in PEM URFCs (Table S1) based on H_2-water cycle, which can only reach a maximum of 74.5% as shown in **Figure 6b**. The RTE above 75% is forbidden for PEM URFCs due to the limiting potentials (U_L) of ORR and OER, which are further restricted by the scaling relationships of the intermediates' binding energy (HO* and HOO*, $\Delta G_{HOO*} \approx \Delta G_{HO*} + 3.2$ eV) along the four-electron reaction pathways (**Figure 6d**).[14-17] In contrast, for the electrochemical cycle of H_2O_2 in UR-HPCC, HOO* is the single intermediate of 2e-ORR and HPOR. Its binding energy (ΔG_{HOO*}) is not limited by any scaling relationships of the intermediates. Therefore, the limiting potential for 2e-ORR and HPOR can reach the thermodynamic equlibrium potential of the reactions, and the UR-HPCC can reach a theoretical 100%-efficiency, rendering this system extremely attractive for energy storage applications (**Figure 6c**). **Figure 6e** shows the RTE as a function of current density in HPEL and FC modes in the first cycle. The highest RTE was achieved at the lowest current density. Along the diagonal line where the charging current and discharging current are equal, the maximum RTE (*ca*. 95.8%) can be achieved at *ca*. 1.00 mA/cm^2, corresponding to 0.72 V and 0.69 V in HPEL and FC modes. During the 15-cycles of the UR-HPCC, its maximum RTE decreased slighly and remained at *ca*. 80%, much higher than that for state-of-the-art H_2-O_2 PEM URFCs (**Figure 6f**).

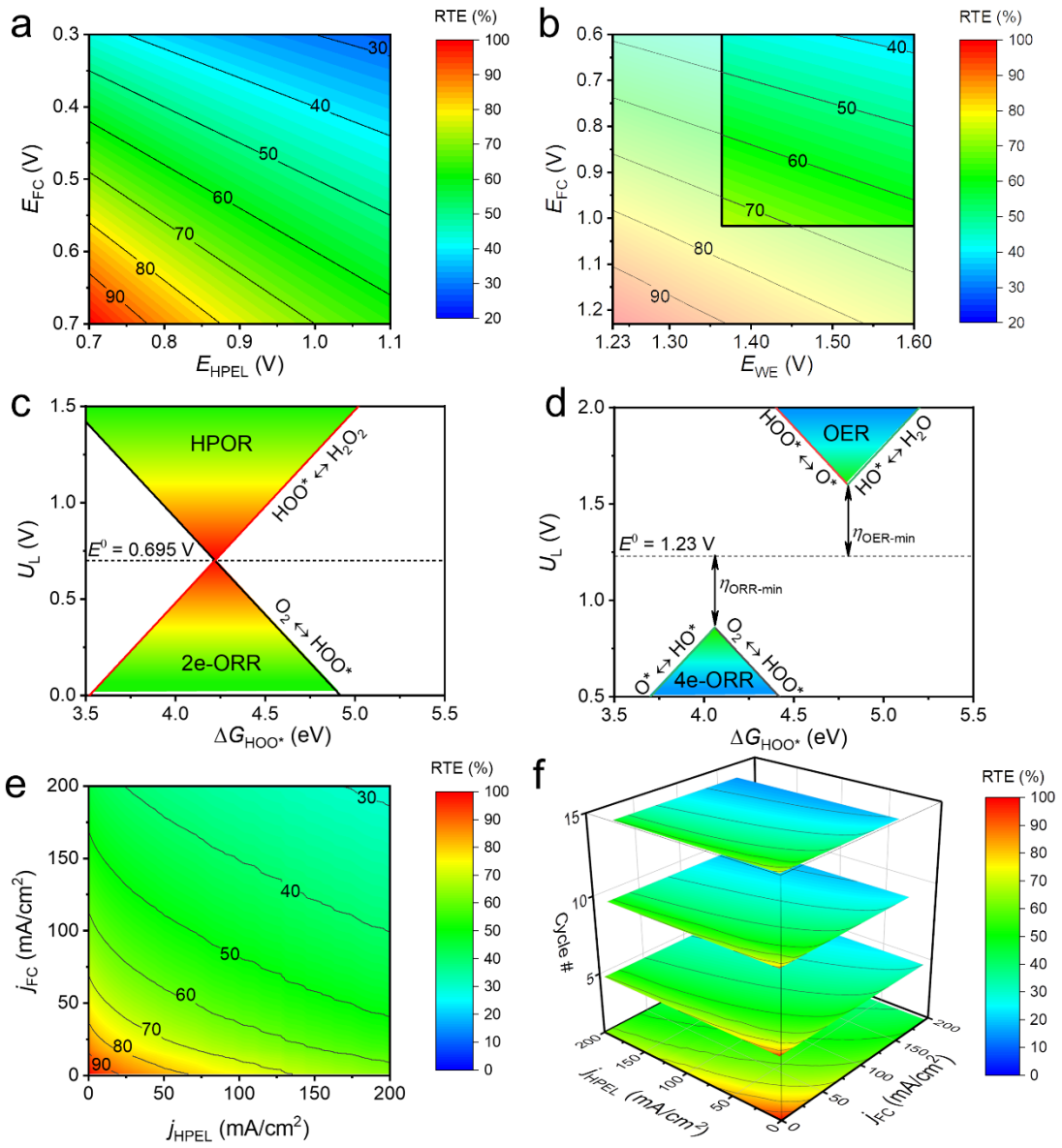

Figure 6. The round-trip efficiency (RTE) of UR-HPCC. 2D contour plot of RTE as a function of cell voltage in (a) UR-HPCC, and (b) URFC with the forbidden region grayed out. (c) The limiting potentials U_L for HPOR and 2e-ORR as a function of ΔG_{HOO*}. (d) U_L for OER and 4e-ORR as a function of ΔG_{HOO*} and the minimum overpotentials $\eta_{OER-min}$ and $\eta_{ORR-min}$. The 2D contour plot of RTE as a function of current density in HPEL and FC modes in (e) the first cycle, and (f) fifteen cycles.

Conclusions

For the first time, we demonstrated a novel PEM UR-HPCC based on the electrochemical cycling of H_2O_2 for renewable energy conversion and storage. A

carbon-based platinum group metal-free (PGM-free) Co-N-C catalyst was used as a bifunctional oxygen electrode catalyst in this UR-HPCC, achieving high RTE, ultra-low overpotentials, and long-term stable operation. The reaction thermodynamics of single-intermediate HPOR/2e-ORR unrestricted by any scaling relationships supports the intrinsic supremacy of UR-HPCC in energy efficiency and reversibility over conventional PEM URFCs. These results indicate that UR-HPCC is highly promising for low-cost grid-scale energy-storage technologies applications. Further improvements in system energy efficiency, catalyst durability and device performance are subject to future research in this emerging field.

Method

Materials. Cobalt (II) chloride ($CoCl_2$, 99.7%, anhydrous, Shanghai Aladdin Biochemical Technology, Co.), aniline (98%, Sigma Aldrich), hydrogen peroxide (H_2O_2, 30 wt%, Alfa Aesar), hydrochloric acid (HCl, 36-38 wt%, analytical reagent grade, SCR, China), nitric acid (HNO_3, 65-68 wt%, analytical reagent grade, SCR, China), ammonium persulfate (APS, 98%, Sigma Aldrich), isopropanol (IPA, > 99.7%, analytical reagent grade, Kermel, China), sulfuric acid (H_2SO_4, 95-98 wt%, analytical reagent grade, SCR, China), deionized water (DI water, Milli-Q, 18.2 MΩ cm at 25 °C), ultrapure nitrogen (N_2, 99.999%), ultrapure oxygen (O_2, 99.999%), carbon black (BlackPearl 2000, Cabot Co.), and a Nafion D521 dispersion (5 wt%, EW = 1100, Chemours) were used as received.

Synthesis of Co-N-C catalyst. Aniline (1.024 g, 11 mmol) was first added into 200 mL of 1 N HCl solution under continuous stirring to form a solution of monomers. A second solution was prepared by adding 1.246 g of 30wt% H_2O_2 solution (11 mmol) and 7.141 g of $CoCl_2$ (55 mmol) into 200 mL of 1 N HCl. The second solution was then added to the aniline solution to initialize the polymerization of aniline and kept at room temperature with constant magnetic stirring at 60 rpm for 4 hours. A dispersion of carbon black was prepared by sonicating 0.200 g of oxidized carbon black (OCB,

pretreated in 70% nitric acid at 80°C for 8 hours, rinsed with DI-water and vacuum dried at 80°C) to a mixture of 100 ml of DI-water and 10 ml of IPA. Then, the dispersion of carbon black was added into the above polymer dispersion while stirring at 600 rpm. After 24 hours, the polymer dispersion was heated to 80°C and concentrated into a dark slurry by continuously stirring at 600 rpm. The obtained slurry was loaded into an alumina combustion boat and heat-treated at 900ºC for one hour in N_2 flow with a ramping rate of 30 ºC/min. The obtained material was ground into a fine powder, treated with a 12 N HCl solution for 24 hours to remove Co-rich phases, rinsed with DI-water, dried in vacuum, and then heat-treated at 900ºC for three hours in N_2 flow with a ramping rate of 30 ºC/min to obtain the Co-N-C catalyst.

The N-C material was synthesized using the same procedure as that for Co-N-C, but without any $CoCl_2$, and the H_2O_2 solution was replaced with APS.

Physical characterization. The Co–N–C catalyst was characterized using a high-resolution transmission electron microscope (TEM, JEM-2100F, JEOL, Japan) equipped with an energy dispersive spectrometer (EDS), and an aberration-corrected high-angle annular dark-field scanning transmission electron microscope (HAADF-STEM, Titan Cubed Themis G2 300, FEI, USA) operated at an accelerating voltage of 300 kV. Powder X-ray diffraction (XRD, D8 ADVANCE A25, Bruker Co., USA) patterns were recorded using a Bruker D8-Advance-A25 diffractometer with Cu Kα radiation over a 2θ range from 5° to 90°. X-ray photoelectron spectroscopy (XPS, Axis Ultra DLD, Kratos Analytical Ltd, UK) was performed using a monochromatic Al Kα source at 150 W without charge compensation.

Electrochemical Measurements. Electrochemical measurements of the 2e-ORR activity were conducted in a five-necked electrochemical cell filled with a 0.5 M H_2SO_4 electrolyte using a bipotentiostat (CHI 760E, CH Instruments, Inc.). A rotating-ring disk electrode (RRDE, Pine Research Instrumentation) with a glassy carbon electrode (GCE, Φ = 5.50 mm, area = 0.2375 cm^2) and a Pt ring was used as the working

electrodes, a graphite rod was used as the counter electrode, and a reversible hydrogen electrode (RHE) was used as the reference electrode.

The catalyst ink was prepared by dispersing 5 mg of catalyst in a mixture of DI water (500 μL), IPA (500 μL), and D521 Nafion dispersion (12 μL, 5 wt%) in a sonication bath for one hour. Electrodes with a catalyst loading of 0.1 mg/cm^2 were prepared by depositing 4.7 μL of the ink onto the GCE. Cyclic voltammograms (CV) were recorded from 0 to 1.0 V *vs*. RHE at a scan rate of 50 mV/s in N_2-saturated 0.5 M H_2SO_4 solution. The 2e-ORR performance was measured in O_2-saturated 0.5 M H_2SO_4 under steady-state conditions by polarizing the working electrode from 1.0 to 0 V *vs*. RHE using 20 mV potential steps and a hold time of 20 s at each step. The rotation rate was 900 rpm. The ring current was measured at a ring potential of 1.3 V *vs*. RHE. The current collection efficiency of the ring electrode (N) is 38%. The H_2O_2 yield (Y_{H2O2}) was calculated using the following equation:

$$Y_{H_2O_2} = 200\% \frac{\left(\frac{I_r}{N}\right)}{\left(I_d + \frac{I_r}{N}\right)} \qquad Eq.1$$

where I_d and I_r are the disk current and the ring current, respectively.

The electrochemical measurements of HPOR activity were conducted in a H-type electrolysis cell. A proton exchange membrane (Nafion® NR211) was used to separate the two compartments of the H-cell. A glassy carbon rotating disk electrode (RDE) (Φ = 5.00 mm, area = 0.1963 cm^2) and a Ag/AgCl (KCl, 3 M) reference electrode were placed in one cell compartment filled with 0.5 M H_2SO_4 and 0.5 M H_2O_2. A graphite rod counter electrode was positioned in the other compartment filled with 0.5 M H_2SO_4. The Ag/AgCl electrode was calibrated to a RHE. Electrodes with a catalyst loading of 0.1 mg/cm^2 were prepared by depositing 3.9 μL of the ink onto the RDE. The HPOR performance was measured by CV from 0 to 1.0 V *vs*. RHE at a scan rate of 50 mV/s and rotation rate of 900 rpm.

Fabrication of MEA and UR-HPRC. The catalyst inks for the bifunctional oxygen electrode were prepared by homogeneously dispersing 10 mg of Co-N-C catalyst in a mixture of DI-water (1.0 mL), IPA (1.3 mL), and D521 Nafion dispersion (215 μL, 5 wt%), and then sonicating for 2 hours. The inks were sprayed onto porous transport layers made of hydrophilic carbon cloth (4 cm^2, *ca*. 0.33 mm in thickness) at 80 °C to form the oxygen electrodes. The catalyst loading was *ca*. 1.7 mg/cm^2. Commercial gas diffusion electrodes with catalyst loading (Fuel Cell Store, 0.2 $mgPt/cm^2$, 20 wt% Pt/C on Sigracet 22 BB carbon paper) were used as the hydrogen electrode and hot-pressed to Nafion NR211 membranes at 120 °C and 5.3 MPa for 5 min to form half-MEAs. The oxygen electrode and the half-MEA were assembled into a full UR-HPCC hardware with 4-cm^2 single-channel (1.27 mm wide and 0.8 mm deep) serpentine flow field graphite plate and sealed with two fluororubber gaskets (200 and 100 μm in thickness) as shown in **Figure S2**.

Cell test in HPEL Mode. The UR-HPCC performance in HPEL mode was evaluated at room temperature and ambient pressure. The experimental set-up is shown in Figure S3a. First, N_2-saturated 0.5 M H_2SO_4 was pumped into the oxygen electrode and circulated between the oxygen electrode and the Boro 3.3 glass bottle at a flow rate of 200 mL/min. The hydrogen electrode was filled with pure H_2 gas to form a reversible hydrogen electrode (RHE). The initial cyclic voltammogram of the oxygen electrode with Co-N-C catalyst was recorded by polarizing the electrode from 0 to 1.0 V at a scan rate of 50 mV/s using a CHI 760E bipotentialstat.

After recording the initial CV, O_2-saturated solution containing 0.5 M H_2SO_4 and 0.5 M H_2O_2 was pumped into the oxygen electrode and circulated at a flow rate of 200 mL/min. Corrosion-resistant Masterflex® Viton tubing was used for the liquid delivery line. A bias voltage was applied between hydrogen and oxygen electrode in a two-electrode configuration using a high-current electrochemical workstation (EnergyLab XM, Solartron Analytical, AMETEK Inc.) equipped with a current booster. Linear sweep AC voltammetry was recorded by increasing the voltage from open cell voltage

(OCV) to 1 V at a scan rate of 5 mV/s, while a 10 kHz AC wave with 5 mV amplitude was applied to measure the real-time high frequency resistance (HFR). The *iR*-corrected cell voltage ($E_{iR\text{-free}}$) was obtained using the following equation:

$$E_{iR-free} = E_{\mathrm{HPEL}} - E_{\mathrm{ohm}} = E_{\mathrm{HPEL}} - j * \mathrm{HFR} \qquad Eq.2$$

where E_{HPEL} is the measured cell voltage, E_{ohm} is the ohmic loss, j is the current density, and HFR is the high frequency resistance.

The voltage efficiency of the cell in HPEL mode ($\mathrm{VE_{HPEL}}$) was calculated according to the following equations:

$$\mathrm{VE_{HPEL}} = \frac{E_{\mathrm{rev-HPOR}}}{E_{\mathrm{HPEL}}} \times 100\% \qquad Eq.3$$

where the $E_{\text{rev-HPOR}}$ is the thermodynamic potential of H_2/H^+/Nafion/O_2/H_2O_2 (E_{rev} = 0.704 V, T = 298.15 K), which was calculated using the Nernst equation:

$$E_{\mathrm{rev-HPOR}} = E^0 + \frac{RT}{nF} \ln\left(\frac{1}{C_{H_2O_2}}\right) \qquad Eq.4$$

where E^0 is the reversible cell potential at the standard conditions with 1 M H_2O_2, R is the ideal gas constant, T is the room temperature, n is the number of electrons transferred (n = 2), F is the Faraday constant, and C_{H2O2} = 0.5 M is the concentration of H_2O_2.

To evaluate the efficiency of hydrogen generation, the generated hydrogen gas at constant *iR*-corrected cell voltages of 0.85, 0.90, 0.95, and 1.00 V was directed to the bubble flow meter (**Figure S3a**). The Faraday efficiency of hydrogen generation ($\mathrm{FE_{H2}}$) was calculated based on the following equation:

$$\mathrm{FE_{H_2}} = \frac{2\left(P - P_{\mathrm{H_2O}}\right)V_{\mathrm{H_2}}F}{RTQ_{\mathrm{total}}} \times 100\% \qquad Eq.5$$

where P is the atmospheric pressure in Taiyuan (92 kPa), P_{H2O} is the saturation vapor pressure of water (kPa) at room temperature, V_{H2} is the volume of fully humidified H_2 produced (L), F is the Faraday constant (96485 C/mol), R is the ideal gas constant (8.314 J/(mol·K)), T is the measured room temperature, and Q_{total} is the amount of charge passed (C).

The stability of the UR-HPCC in HPEL mode was evaluated using the galvanostatic method at a fixed current density of 50 mA/cm^2. The flow rate of the anolyte solution was 50 mL/min. The electrolyte containing 0.5 M H_2SO_4 and 0.5 M H_2O_2 was replenished every four hours to maintain the concentration.

Cell test in FC mode. The cell was tested on a Scribner 850e fuel cell test station at a cell temperature of 25 °C under H_2/O_2 flow at 200 sccm and 100% relative humidity (RH) and ambient pressure. The experimental set-up is shown in Figure S3b. The steady-state fuel cell polarization curves were recorded by polarizing the cell from OCV to 0 V, using 0.02 V steps and 20 s hold time at each voltage. The *iR*-corrected cell voltage ($E_{iR\text{-free}}$) was obtained using the following equation:

$$E_{iR-free} = E_{\mathrm{FC}} + E_{\mathrm{ohm}} = E_{\mathrm{FC}} + j * \mathrm{HFR} \qquad Eq.6$$

where E_{FC} is the measured cell voltage in FC mode, E_{ohm} is the ohmic loss, j is the current density, and HFR is the high frequency resistance.

The voltage efficiency of the cell operating in FC mode (VE_{FC}) were calculated according to the following equations:

$$\mathrm{VE_{FC}} = \frac{E_{\mathrm{rev-2eORR}}}{E_{\mathrm{FC}}} \times 100\% \qquad Eq.7$$

where the $E_{\mathrm{rev\text{-}2eORR}}$ is the thermodynamic potential of two electrode oxygen reduction reaction (2e-ORR: $E_{\mathrm{rev\text{-}2eORR}}$ = 0.695 V, T = 298.15 K) assuming the local concentration of H_2O_2 is 1 M.

DI-water was pumped into the oxygen electrode at a rate of 10 mL/min in addition to the oxygen gas flow to wash out the generated H_2O_2 (**Figure S3b**). The amount of H_2O_2 collected was determined using a standard potassium permanganate titration process, according to the following reaction:

$$2\mathrm{MnO_4^-} + 5\mathrm{H_2O_2} + 6\mathrm{H^+} \rightarrow 2\mathrm{Mn^{2+}} + 8\mathrm{H_2O} + 5\mathrm{O_2}$$

where 0.5 M H_2SO_4 was used as the H^+ source. When decolorization occurs, the molar mass of collected H_2O_2 (n_{H2O2}) is:

$$n_{\mathrm{H_2O_2}} = \frac{5C_{\mathrm{KMnO_4}}V_{\mathrm{KMnO_4}}}{2} \qquad Eq.8$$

where C_{KMnO4} (1 M) and V_{KMnO4} are the molarity and volume of $KMnO_4$ solution used for the titration process, respectively.

The Faradaic efficiency for H_2O_2 synthesis (FE_{H2O2}) can be calculated using following equation:

$$\mathrm{FE}_{\mathrm{H_2O_2}} = \frac{2Fn_{\mathrm{H_2O_2}}}{Q} \times 100\% \qquad Eq.9$$

where F is the Faraday constant, Q is the total charge when collecting n_{H2O2} of H_2O_2.

The stability of the UR-HPCC in FC mode was evaluated using the galvanostatic method at a fixed current density of 50 mA/cm^2. It should be noted that since the hydrophilic carbon cloth was used for the oxygen electrode gas diffusion layer (GDL), flooding is easy to occur. During the stability test, the oxygen electrode was purged with dry nitrogen at 200 sccm for 30 min every 2 hours.

UR-HPCC cyclability test. The UR-HPCCs were periodically cycled between HPEL mode and FC mode every one hour to evaluate its reversibility. LSV curves at HPEL mode and steady-state polarization curves at FC mode were recorded at the conditions specified above. The cell stability was evaluated using the galvanostatic method at a fixed current density of 50 mA/cm^2. When switching from HPEL mode to FC mode, the oxygen electrode was rinsed with DI-water, followed by purging both electrodes with dry N_2 at 200 sccm for 30 min. When switching from FC mode to HPEL mode, the H_2/O_2 supply was stopped first and the electrolyte containing 0.5 M H_2SO_4 and 0.5 M H_2O_2 was supplied on the oxygen electrode at a flow rate of 200 mL/min.

References and Notes:

Acknowledgments:

Financial support from the State Key Laboratory of Coal Conversion, Institute of Coal Chemistry, Chinese Academy of Sciences is greatly appreciated. This work was financially supported by the autonomous research project of SKLCC (Grant No.

2021BWZ006), ICC CAS (Grant No. 2020SC001), and Shanxi Province grant 2020SHB006. The authors would like to thank Dr. Zhi Cao, and Dr. Baoliang Lv for their assistance during the project.

Competing interests:

Pending patent of a unitized regenerative hydrogen peroxide cycle cell (CN.202111123206.X).

Data availability:

All data are available in the main text and the supplementary materials.

1. Gür, T. M. Review of electrical energy storage technologies, materials and systems: challenges and prospects for large-scale grid storage. *Energy Environ. Sci.* **11**, 2696-2767 (2018).
2. Pellow, M. A., Emmott, C. J. M., Barnhart, C. J. & Benson, S. M. Hydrogen or batteries for grid storage? A net energy analysis. *Energy Environ. Sci.* **8**, 1938-1952 (2015).
3. Duan, C. *et al.* Highly efficient reversible protonic ceramic electrochemical cells for power generation and fuel production. *Nat. Energy* **4**, 230-240 (2019).
4. Park, S., Shao, Y., Liu, J. & Wang, Y. Oxygen electrocatalysts for water electrolyzers and reversible fuel cells: status and perspective. *Energy Environ. Sci.* **5**, 9331-9344 (2012).
5. Hunsom, M., Kaewsai, D. & Kannan, A. M. Recent developments in bifunctional air electrodes for unitized regenerative proton exchange membrane fuel cells – A review. *Int. J. Hydrogen Energy* **43**, 21478-21501 (2018).
6. Dresp, S. *et al.* An efficient bifunctional two-component catalyst for oxygen reduction and oxygen evolution in reversible fuel cells, electrolyzers and rechargeable air electrodes. *Energy Environ. Sci.* **9**, 2020-2024 (2016).
7. Davis, S. J. *et al.* Net-zero emissions energy systems. *Science* **360**, eaas9793 (2018).
8. Regmi, Y. N. *et al.* A low temperature unitized regenerative fuel cell realizing 60% round trip efficiency and 10 000 cycles of durability for energy storage applications. *Energy Environ. Sci.* **13**, 2096-2105 (2020).
9. Wang, Y., Leung, D. Y. C., Xuan, J. & Wang, H. A review on unitized regenerative fuel cell technologies, part-A: Unitized regenerative proton exchange membrane fuel cells. *Renew. Sustain. Energy Rev.* **65**, 961-977 (2016).
10. Peng, X. *et al.* Hierarchical electrode design of highly efficient and stable unitized regenerative fuel cells (URFCs) for long-term energy storage. *Energy Environ. Sci.* **13**, 4872-4881 (2020).

11. Lim, A. *et al.* Low-loading IrO_2 supported on Pt for catalysis of PEM water electrolysis and regenerative fuel cells. *Appl. Catal. B Environ.* **272**, 118955 (2020).
12. Lim, A. *et al.* Polymer electrolyte membrane unitized regenerative fuel cells: Operational considerations for achieving high round trip efficiency at low catalyst loading. *Appl. Catal. B Environ.* **297**, 120458 (2021).
13. Lee, W. H. *et al.* High crystallinity design of Ir-based catalysts drives catalytic reversibility for water electrolysis and fuel cells. *Nat. Commun.* **12**, 4271 (2021).
14. Wan, H., Jensen, A. W., Escudero-Escribano, M. & Rossmeisl, J. Insights in the oxygen reduction reaction: From metallic electrocatalysts to diporphyrins. *ACS Catal.* **10**, 5979-5989 (2020).
15. Kulkarni, A., Siahrostami, S., Patel, A. & Nørskov, J. K. Understanding catalytic activity trends in the oxygen reduction reaction. *Chem. Rev.* **118**, 2302-2312 (2018).
16. Baran, J. D., Grönbeck, H. & Hellman, A. Analysis of porphyrines as catalysts for electrochemical reduction of O_2 and oxidation of H_2O. *J. Am. Chem. Soc.* **136**, 1320-1326 (2014).
17. Koper, M. T. M. Theory of multiple proton-electron transfer reactions and its implications for electrocatalysis. *Chem. Sci.* **4**, 2710-2723 (2013).
18. Ding, R. L., Chang; Yang, Jie; Liu, Shanshan; Xu, Qinchao; Li, Junfen; Yin, Xi;. Low-voltage hydrogen peroxide electrolyzer for highly efficient power-to-hydrogen conversion. *ChemRxiv* (2021). DOI: 10.26434/chemrxiv-2021-9dmp4
19. Artyushkova, K. *et al.* Density functional theory calculations of XPS binding energy shift for nitrogen-containing graphene-like structures. *Chem. Commun.* **49**, 2539-2541 (2013).
20. Sun, Y. *et al.* Activity–selectivity trends in the electrochemical production of hydrogen peroxide over single-site metal–nitrogen–carbon catalysts. *J. Am. Chem. Soc.* **141**, 12372-12381 (2019).
21. Guo, X. *et al.* Simultaneously achieving high activity and selectivity toward two-electron O_2 electroreduction: The power of single-atom catalysts. *ACS Catal.* **9**, 11042-11054 (2019).
22. Gao, J. *et al.* Enabling direct H_2O_2 production in acidic media through rational design of transition metal single atom catalyst. *Chem* **6**, 658-674 (2020).
23. Wang, N., Ma, S., Zuo, P., Duan, J. & Hou, B. Recent progress of electrochemical production of hydrogen peroxide by two-electron oxygen reduction reaction. *Adv. Sci.* **8**, 2100076 (2021).
24. Jung, E. *et al.* Atomic-level tuning of Co–N–C catalyst for high-performance electrochemical H_2O_2 production. *Nat. Mater.* **19**, 436-442 (2020).
25. Siahrostami, S. *et al.* Two-dimensional materials as catalysts for energy conversion. *Catal. Lett.* **146**, 1917-1921 (2016).
26. Wang, Z. *et al.* Hydrogen peroxide generation with 100% faradaic efficiency on metal-free carbon black. *ACS Catal.* **11**, 2454-2459 (2021).